

Three-dimensional spin liquid state in the frustrated $S = 1/2$ Heisenberg garnet $\text{NaCa}_2\text{Cu}_2(\text{VO}_4)_3$

Y. Alexanian,^{1,*} R. Kumar,² H. Zeroual,² B. Bernu,³ L. Mangin-Thro,¹ R. S. Stewart,⁴
J. M. Wilkinson,⁴ P. L. Paulose,⁵ F. Bert,² P. Mendels,² B. Fåk,¹ and E. Kermarrec²

¹*Institut Laue Langevin, 38042 Grenoble, France*

²*Université Paris-Saclay, CNRS, Laboratoire de Physique des Solides, 91405, Orsay, France*

³*Sorbonne Université, CNRS, Laboratoire de Physique Théorique de la Matière Condensée, 75252 Paris Cedex 05, France*

⁴*ISIS Neutron and Muon Source, Rutherford Appleton Laboratory, Didcot OX11 0QX, United Kingdom*

⁵*Department of Condensed Matter Physics and Materials Science, TIFR, Mumbai 400 005, India*

(Dated: January 9, 2025)

Three-dimensional quantum spin liquids have remained elusive, hindered by reduced quantum fluctuations from larger lattice connectivity inherent to high-dimensional systems. Here, we investigate the remarkable persistence of dynamical short-range magnetic correlations in the nearly body-centered cubic garnet $\text{NaCa}_2\text{Cu}_2(\text{VO}_4)_3$ down to $T = 50$ mK, two orders of magnitude below its Curie-Weiss temperature. Using a combination of neutron and muon spectroscopies plus numerical simulations, we demonstrate that a spin-liquid phase emerges from the interplay of strongly frustrated exchange interactions and subtle temperature-dependent Jahn-Teller spin-lattice effects.

Quantum spin liquids (QSLs) are long-range entangled states of matter, that evade thermodynamic phase transitions and remain dynamically disordered due to quantum fluctuations [1–3]. While one-dimensional (1D) QSLs are well-established [4–7], they appear in more constrained forms compared to the diverse theoretical predictions for higher dimensions. Over the past few decades, extensive research has focused on two-dimensional (2D) QSL candidates built on triangular lattice motifs [8–10]. The mineral herbertsmithite $\text{ZnCu}_3(\text{OH})_6\text{Cl}_2$ stands out as the most promising realization of the $S = 1/2$ Kagome Heisenberg antiferromagnet exhibiting several defining characteristics of QSLs [11, 12]. Conversely, three-dimensional (3D) QSL candidates have long been scarce, since the higher lattice connectivity limit the degeneracy of low energy states necessary for QSL formation. The recent growing variety of experimentally discovered low-connectivity three-dimensional (3D) frustrated lattices (hyperkagome [13, 14], pyrochlore [15, 16], trillium [17–19], etc.) opens new perspectives on this long-standing challenge [20–25]. Rare-earth-based pyrochlore oxides provide noteworthy cases, with exotic ground states stabilized by strong anisotropic interactions and large magnetic moments [26]. Nevertheless, the complex nature of $4f$ electron states and their small magnetic energy scale complicate the identification of the key mechanisms underlying their low-temperature behavior. While a consensus on the existence of a true 3D QSL has thus not yet been reached, Ce-based [27, 28] and charge disordered Tb-based pyrochlores currently show great promises [29, 30].

An alternative approach to realize a 3D QSL involves frustration arising from multiple competing exchange within seemingly simpler lattices. A few recent candidates, such as $\text{Ca}_{10}\text{Cr}_7\text{O}_{28}$ [31, 32] and $\text{PbCuTe}_2\text{O}_6$ [33, 34], illustrate how these competing interactions can stabilize unconventional magnetic states. Also very

promising is the garnet family $\text{X}_3\text{Y}_2(\text{ZO}_4)_3$ where atoms at the Y -site form a body-centered cubic (bcc) lattice [35, 36]. In $\text{Ca}_3\text{Cu}_2\text{GeV}_2\text{O}_{12}$, the Cu^{2+} spins— $1/2$ (naturally prone to quantum fluctuations) realize the bcc lattice, preventing long-range magnetic ordering down to $T = 0.35$ K [37]. However, it has a low magnetic energy scale ($\theta_{\text{CW}} = -0.93$ K), and the role of paramagnetic impurities in determining its ground state remains unclear.

Interestingly, several members of this magnetic garnet family were investigated long before the concept of QSLs emerged [38–42]. One notable example is the copper-based material $\text{NaCa}_2\text{Cu}_2(\text{VO}_4)_3$, where Cu^{2+} ions occupy a bcc lattice at room temperature. Below $T \approx 250$ K, the crystallographic structure undergoes a small structural transition to a tetragonal phase ($c/a = 0.985$), likely driven by cooperative Jahn-Teller effects [40]. Early macroscopic studies revealed magnetic correlations from $T = 25$ K, but no long-range magnetic order was observed down to at least $T = 0.2$ K [42].

This is particularly intriguing in light of recent numerical studies of the $J_1 - J_2 - J_3$ bcc Heisenberg model [43, 44]. No classical spin liquid phase is stabilized and it is only in the quantum $S = 1/2$ limit that a small region of the ground-state phase diagram is found to be paramagnetic. The close proximity of $\text{NaCa}_2\text{Cu}_2(\text{VO}_4)_3$ to a perfect bcc lattice and the absence of magnetic order in this system thus warrant further investigations.

In this study, we demonstrate that the quantum spins of $\text{NaCa}_2\text{Cu}_2(\text{VO}_4)_3$ remain highly dynamic down to at least $T = 0.05$ K. Our data further reveal temperature-dependent Jahn-Teller effects along with a subtle interplay of quasi-elastic and inelastic dynamics. Based on a numerical analysis, we attribute this behavior to strong magnetic frustration among incipient ferromagnetic spin chains driven by the spin-lattice effects. These competing interactions ultimately promote the unconventional three-dimensional spin liquid state of $\text{NaCa}_2\text{Cu}_2(\text{VO}_4)_3$.

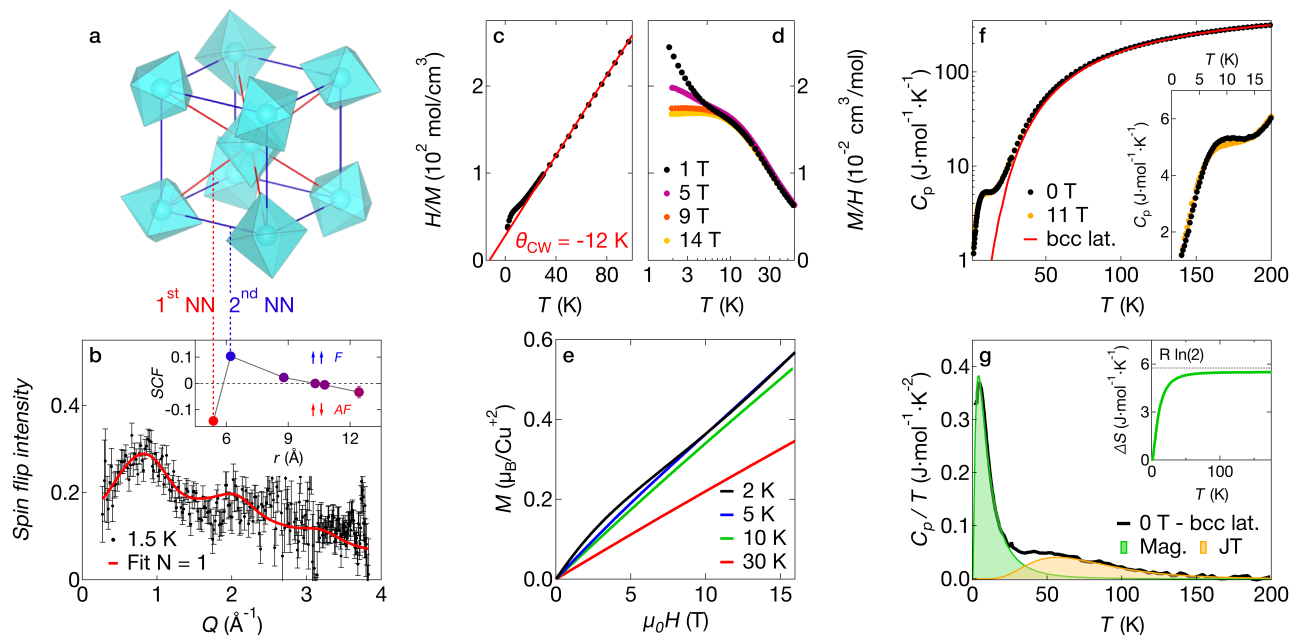


FIG. 1. **Short range magnetic correlations in $\text{NaCa}_2\text{Cu}_2(\text{VO}_4)_3$.** **a** Perfect bcc lattice of Cu^{2+} ions in $\text{NaCa}_2\text{Cu}_2(\text{VO}_4)_3$ at room temperature. Oxygens O^{2-} sits at the polyhedral vertices. First- and second nearest-neighbors are indicated by red and blue lines, respectively. **b** Spin-polarized neutron scattering intensity at $T = 1.5$ K. The red line shows the SPINVERT refinement using isotropic spins. Inset: spin correlation function (SCF) extracted from the refinement. **c** Inverse magnetic susceptibility with its high-temperature fit (50 K to 250 K). **d** Magnetic susceptibility measured at various magnetic field. **e** Magnetization up to $\mu_0 H = 16$ T at different temperatures. **f** Temperature dependence of the specific heat at 0 T and 11 T. The bcc lattice (bcc lat.) contribution is obtained from the measurements of the non-magnetic analogue $\text{NaCa}_2\text{Mg}_2(\text{VO}_4)_3$ (see Methods). **g** Zero-field specific heat subtracted from the bcc lattice contribution (black line), and fits of the magnetic (Mag., green area) and Jahn-Teller (JT, orange area) contributions (see Methods). Inset: temperature variation of the magnetic entropy, obtained from the integration of the magnetic specific heat.

RESULTS

Polarized neutron diffraction and bulk characterisation : evidences for magnetic correlations

In Fig. 1, we present experimental evidences that $\text{NaCa}_2\text{Cu}_2(\text{VO}_4)_3$ exhibits a correlated magnetic state without long range order. Our polycrystalline samples were synthesized via solid-state reaction (see Methods), and their crystallographic structure was checked by X-ray diffraction at $T = 298$ K (see Fig. 1a and Supplementary Information A).

Magnetic correlations are first revealed through our polarized neutron diffraction measurements at $T = 1.5$ K recorded on D7 at ILL (Fig. 1b). No magnetic Bragg peaks are observed, but oscillations in the spin-flip intensity with a prominent maximum at $Q = 0.9 \text{ \AA}^{-1}$ are evident. This establishes the absence of long-range order but the presence of magnetic correlations, no longer visible at $T = 300$ K (see Supplementary Material B). We performed Monte Carlo simulations using the SPINVERT software [45] with $N \times N \times N$ cubic unit cells of isotropic spins to characterize the correlations. Good agreement was achieved for $N = 1$, while no significant

improvement was obtained by increasing N or introducing the tetragonal distortion. Notably, models restricted to Ising or XY spins did not reproduce the observed data. We found antiferromagnetic correlations for first nearest-neighbors and ferromagnetic ones for second nearest-neighbors, located respectively at 5.38 \AA and 6.21 \AA , and rapidly decreasing beyond these distances. The expected magnetic scattering from single crystals calculated with the SCATTY software [46] is shown in Supplementary Material B.

Signatures of magnetic interactions affecting the system at much higher temperatures - and hence magnetic frustration - are evident in our inverse magnetic susceptibility data shown in Fig. 1c. The curve follows a Curie-Weiss law down to $T = 30$ K, below which it begins to deviate from linearity. Fitting the high-temperature range above 50 K yields a Curie-Weiss temperature of $\theta_{\text{CW}} = -12$ K, indicating dominant antiferromagnetic interactions. Notably, another change of slope is observed at lower temperatures, between $T = 5$ K to 10 K. As shown in Fig. 1d, the magnetic susceptibility becomes field-dependent at such temperatures, saturating only above 9 T. Subtracting the high-field from low-field data rules out paramagnetic impurities, as the result does

not follow a Curie law. Further insight comes from our magnetization measurements up to $\mu_0 H = 16$ T across temperatures from $T = 2$ K to $T = 30$ K (Fig. 1e). The magnetization evolves smoothly at each temperature, and reaches $0.56 \mu_B$ per Cu^{2+} ion at 2 K and 16 T, lower than the expected $gS\mu_B = 1 \mu_B$ and far from saturation. Additionally, a distinct feature emerges at low magnetic field for $T = 2$ K, with a significantly faster polarization of some of the spins up to 6 T, as compared to the $T = 5$ K data. This behavior correlates with the magnetic field dependence of the susceptibility below $T = 5$ K and indicates the presence of a second magnetic energy scale of ferromagnetic sign.

Specific heat data are presented in Fig. 1f. A clear departure from the bcc lattice contribution (derived from measurements on the non-magnetic analogue $\text{NaCa}_2\text{Mg}_2(\text{VO}_4)_3$, see Methods) is evident below $T = 50$ K: this is another indication of magnetic correlations. Consistent with the absence of saturation in our magnetization data, only a marginal response to a magnetic field of $\mu_0 H = 11$ T is observed. The specific heat subtracted from the bcc lattice signal and divided by the temperature (Fig. 1g) reveals a pronounced peak around 5 K with a long tail extending up to $T = 200$ K. Since signatures of magnetic correlations are only evident below $T = 50$ K in both the specific heat and magnetic susceptibility data, we attribute the long tail to another lattice effect. This is not surprising since $\text{NaCa}_2\text{Cu}_2(\text{VO}_4)_3$ is Jahn-Teller active below $T = 250$ K, unlike the perfectly bcc non-magnetic analogue $\text{NaCa}_2\text{Mg}_2(\text{VO}_4)_3$ from which we extracted the initial lattice contribution. To estimate the magnetic specific heat, we fit the magnetic and Jahn-Teller contributions with two asymmetric functions (see Methods). The integration of the magnetic signal reaches 95% of $R \ln(2)$ at $T = 50$ K. This simple, phenomenological, analysis suggests that all the expected magnetic entropy is recovered and therefore no magnetic ordering is expected at lower temperatures.

Muon spin relaxation: a dynamical state down to 50 mK

To confirm the absence of long-range order or any other spin freezing at lower temperatures, we performed muon spin relaxation down to 0.05 K, see Fig. 2. The temperature evolution of a selection of zero-field relaxation from 300 K down to 0.05 K is shown in Fig. 2a. At 300 K, the Cu^{2+} moments are in a fast fluctuating regime and the Gaussian shape of the relaxation at early times reflect the nuclear static field. At 50 mK, longitudinal field measurements quickly recover almost the full asymmetry, confirming the nuclear static origin of the Gaussian relaxation. Above 50 G, a slowly exponentially decaying relaxation points to the presence of fast, persistent, spin dynamics of electronic origin (Fig. 2b). A first estimate of the fluctuation frequency ν can be derived from

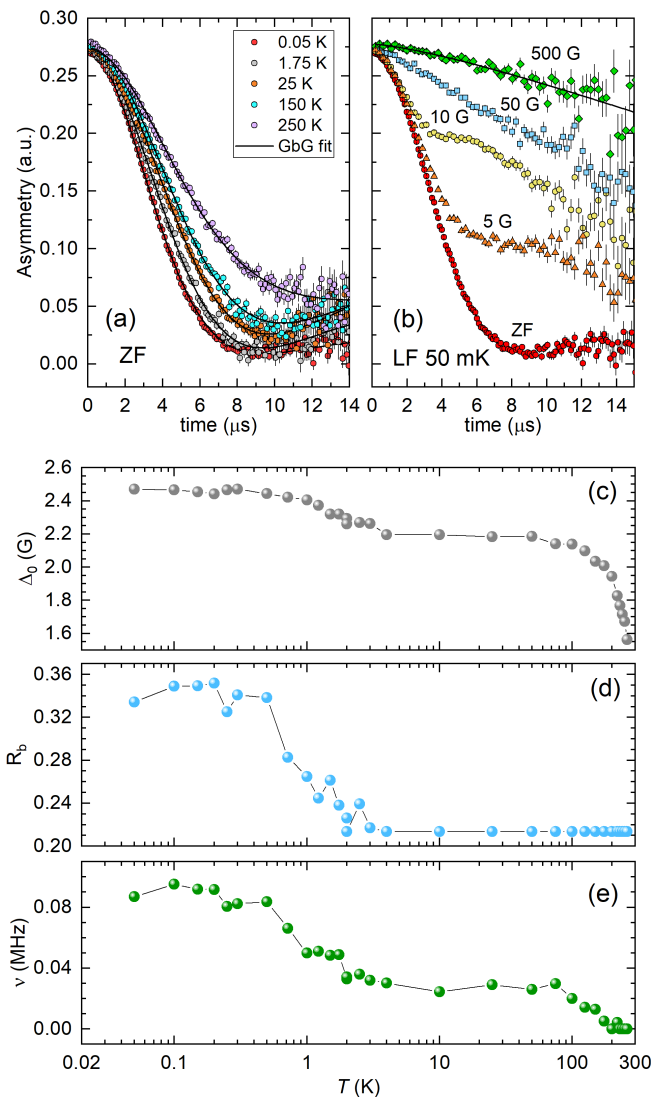


FIG. 2. **Muon spin relaxation in $\text{NaCa}_2\text{Cu}_2(\text{VO}_4)_3$.** **a** Temperature dependence of the zero-field relaxation. Lines are fits to a dynamical Gaussian-broadened-Gaussian model (GbG) (see text). **b** Relaxation measured under longitudinal applied fields, from 0 (ZF) to 500 G, at $T = 50$ mK. Under 500 G, the residual relaxation reflects fast spin dynamics. Black line is a stretched exponential fit. **c**, **d** and **e**: evolution in temperature of the extracted fitting parameters Δ_0 , R^b and ν (see eq. 1).

a stretched exponential fit of the relaxation, $Ae^{-(\lambda t)^\beta}$. Such fit of the 500 G data leads to $\lambda = 0.024(1) \mu\text{s}^{-1}$, which, assuming a fluctuating moment for a Cu^{2+} ion of $1 \mu_B$, gives $\nu \simeq 2\gamma_\mu^2 \Delta^2 / \lambda = 44(2)$ GHz using the Redfield formula (see Methods for details). This confirms the fast fluctuation regime with $\nu \gg \gamma_\mu \Delta$. In conclusion, our muSR data proves the absence of any spin freezing of the Cu^{2+} moments and fully qualifies the garnet $\text{NaCa}_2\text{Cu}_2(\text{VO}_4)_3$ as a quantum spin liquid candidate down to 50 mK.

We now turn to the evolution of the zero-field relax-

ation over the whole 0.05 K to 300 K range. We found that the best modelization of the data was obtained with the dynamical Gaussian-broadened-Gaussian Kubo Toyabe function [47, 48]. The pronounced Gaussian shape coupled to the singularly reduced local dip near 8 μ s to 10 μ s strongly suggest to use the quasi-static approximation with the following expression [47]:

$$P_{\text{GbG}}(t) = \frac{1}{3} \exp\left(-\frac{2}{3}\nu t\right) + \frac{2}{3} \left(\frac{1}{1 + R_b^2 \gamma_\mu^2 \Delta_0^2 t^2}\right)^{3/2} \left(1 - \frac{\gamma_\mu^2 \Delta_0^2 t^2}{1 + R_b^2 \gamma_\mu^2 \Delta_0^2 t^2}\right) \times \exp\left[-\frac{\gamma_\mu^2 \Delta_0^2 t^2}{2(1 + R_b^2 \gamma_\mu^2 \Delta_0^2 t^2)}\right] \quad (1)$$

This function models a relaxation due to a homogeneous disorder, yet within a disordered static scenario of a collection of Gaussian field distributions. This results in a three parameters model: the width of the static field Gaussian distribution Δ_0 , the ratio $R_b = \Delta_G/\Delta_0$ where Δ_G is the standard deviation of the Gaussian-weighted initial distribution, and the fluctuation frequency ν characterizing the dynamics. The muon gyromagnetic ratio is $\gamma_\mu = 851.4 \text{ Mrad}\cdot\text{T}^{-1}$.

This function successfully captures the behavior of the relaxation over the whole temperature range, and the dependence of the three parameters are shown in Fig. 2b. From 300 K to 50 K, the distribution width Δ_0 due to nuclear fields increases with temperature up to 2.2 G. This is somewhat unusual as this value depends on the structural positions of neighboring atoms. Here, this naturally reflects the smooth evolution of the structural distortion between 250 and 50 K [40]. Thus, our muon data appear to be strongly sensitive to the Jahn-Teller driven structural transition below 250 K that clearly modify the local environment of the muon, and then the value of Δ_0 . Interestingly, Δ_0 is found to increase again just below 10 K, where the magnetic correlations set in, which hints at a subtle atomic and/or orbital modification. The parameter R_b essentially shares the same temperature dependence as Δ_0 , with values ranging from ~ 0.2 to 0.35, indicating a moderate structural disorder, likely caused by the Na/Ca double occupation of the same crystallographic site (Wyckoff 24c) and Jahn-Teller vibrational modes. This provides a natural explanation for the multiple muon environments captured by the Gaussian-broadened-Gaussian model. Finally, the parameter ν is important as it directly probes the dynamics probed by the muon. Although ν and Δ_0 seem highly correlated, our tests to fix one of them considerably degrade the quality of the fit, and thus we conclude to the physical relevance of both parameters. At first, ν slightly increases upon cooling from 300 K and levels off below ~ 50 K. Similarly to Δ_0 , a second increase occurs below 10 K and then ν remains constant below 0.5 K. We note the tiny

anomaly around 0.2 K for all parameters, reminiscent of the observation of a kink in magnetic susceptibility [42] and interpreted as indication of magnetic order. Our muon data, sensitive to both structural change and magnetism, rather shows a subtle effect which does not lead to any spin freezing or ordering. Instead, they support the presence of a correlated regime below 10 K, in agreement with polarized neutron diffraction, yet with Cu^{2+} moments which remain fully dynamics down to 50 mK. Furthermore, our data reveal the existence of two types of excitations with different timescales: (i) a slow dynamic ascribed to the fluctuations of nuclear fields and linked to the Jahn-Teller vibrations, and (ii) fast fluctuations relevant to the Cu^{2+} electronic moments.

Inelastic neutron scattering: dual quasi-elastic and inelastic response

We investigated the spin excitation spectra of $\text{NaCa}_2\text{Cu}_2(\text{VO}_4)_3$ with inelastic neutron scattering measurements recorded on LET at ISIS (Fig. 3). Data at $T = 1.5$ K with an incident neutron energy of $E_i = 3.7$ meV and $E_i = 12.12$ meV are presented in Figs. 3a,b. A very broad excitation is visible in the dynamical neutron scattering function $S(Q, E)$ below 3 meV, while no scattered intensity is detected above, up to 9 meV. The overall intensity of this large feature decreases with increasing Q (indicating a magnetic origin), is gapless within our energy resolution ($\Delta E \simeq 50 \mu\text{eV}$), and exhibits dispersive behavior. As the temperature increases, the intensity decreases rapidly, essentially vanishing at $T = 20$ K (see Fig. 3d-f), while the scattering becomes quasi-elastic at $T = 300$ K in the paramagnetic and uncorrelated regime (see Fig. 3g and Supplementary Information B). This provides clear evidence that the excitation spectrum observed at low temperatures is intrinsically linked to the magnetic correlations.

The broad excitation observed at $T = 1.5$ K (Fig. 3) is intriguing. On one hand, it does not fully resemble the dispersionless dome-like feature often seen in gapless quantum spin liquid candidates [12, 49, 50]. On the other hand, there is no evidence for incipient magnetic order down to $T = 50$ mK, which could give rise to highly damped spin waves and explain its dispersive nature. To gain a better understanding, we quantitatively characterize it by fitting successive energy cuts, integrated in a momentum window $Q \pm 0.05 \text{ \AA}^{-1}$ (see Methods), for $T = 1.5$ K and $T = 20$ K (cuts for $Q = 0.85 \text{ \AA}^{-1}$ are shown in Figs. 3c,f; some others are shown in Supplementary Material C). Clearly, the data cannot be described by a single peak of any shape due to the lack of intensity around $E \approx 1$ meV. Instead, a dual response is necessary to accurately reproduce the signal. We achieve very good agreement with the data up to at least $Q = 2.25 \text{ \AA}^{-1}$ with

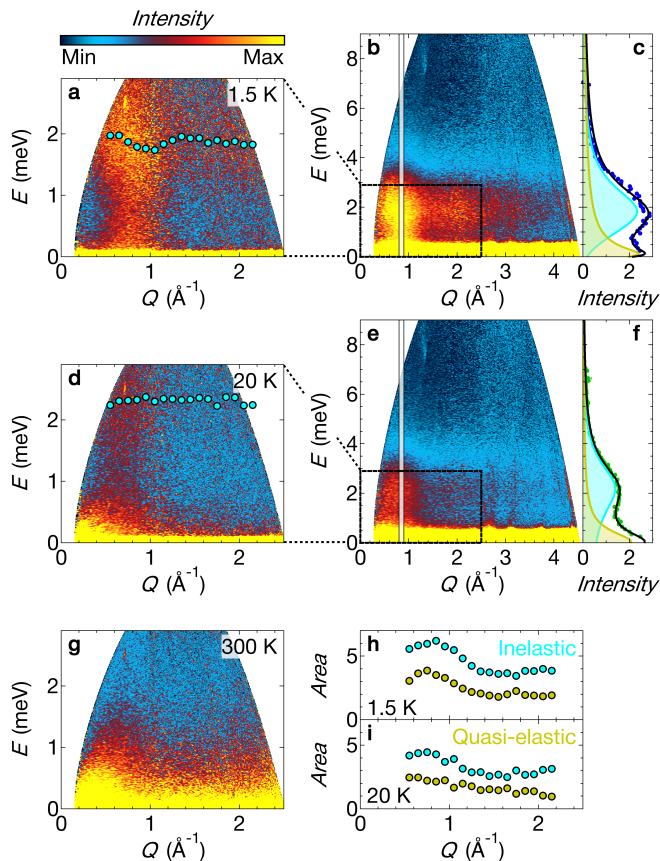


FIG. 3. **Magnetic excitations of $\text{NaCa}_2\text{Cu}_2(\text{VO}_4)_3$.** **a,d,g** Color maps of the neutron intensity measured with an incident neutron beam energy of $E_i = 3.7$ meV at (a) $T = 1.5$ K, (d) $T = 20$ K, and (g) $T = 300$ K. Light blue dots on panels (a,d) represents the characteristic energy E_c of the inelastic contribution (see below). **b,e** Similar maps measured with $E_i = 12.12$ meV at (b) $T = 1.5$ K, and (e) $T = 20$ K. The momentum and energy ranges for the measurements shown in panels (a) and (d) are indicated by the black box. **c,f** Constant momentum cuts integrated over the momentum range 0.8 \AA^{-1} to 0.9 \AA^{-1} (white boxes in panels (b,e)) at (c) $T = 1.5$ K and (f) $T = 20$ K. Cuts are fitted by a quasi-elastic (yellow) and an inelastic (light blue) contributions of characteristic energy E_c (see text). **h,i** Momentum evolution of the areas of the quasi-elastic (yellow) and inelastic (light blue) contributions at (h) $T = 1.5$ K and (i) $T = 20$ K, derived from the fits of panels (c) and (f) and similar ones at other momentum values.

the scattering function:

$$\begin{aligned}
 S(E, T) &= \frac{1}{1 - \exp(-E/k_B T)} [\chi''_{\text{Qel}}(E) + \chi''_{\text{Inel}}(E)]; \\
 \chi''_{\text{Qel}}(E) &= \frac{z\gamma E}{E^2 + \gamma^2}; \\
 \chi''_{\text{Inel}}(E) &= \left[\frac{Z\Gamma}{(E - E_c)^2 + \Gamma^2} - \frac{Z\Gamma}{(E + E_c)^2 + \Gamma^2} \right].
 \end{aligned} \tag{2}$$

The first term of Eq. 2 represents a quasi-elastic signal

of amplitude z and linewidth γ . This accounts for the gapless part of the scattering. The second term corresponds to an inelastic contribution of amplitude Z , characteristic energy E_c and linewidth Γ . As revealed by the momentum dependence of E_c (shown in light blue dots in Figs. 3a,d.), this signal is dispersive at $T = 1.5$ K and becomes dispersionless already at $T = 20$ K, reflecting weaker magnetic correlations. In Figs. 3h,i, we show the momentum modulation of the energy integrated intensity of the two excitations (defined as the energy integration in the range 0 meV to 9 meV of both contributions to $S(E, T)$, see Methods for details). At 1.5 K, both the quasi-elastic and inelastic energy integrated intensities closely track the intensity modulation observed in polarized neutron diffraction (Fig. 1b). Notably, the maximum integrated intensity occurs at $Q \sim 0.9 \text{ \AA}^{-1}$, with a second local maximum observed for $Q \sim 2 \text{ \AA}^{-1}$. This indicates that a significant portion of the energy-integrated signal observed on the D7 spectrometer is indeed quasi-elastic and inelastic, suggesting that spin dynamics still persist on a much shorter timescale than that probed by μSR .

High-temperature series expansion: strongly frustrated spin chains

We analyse the bulk magnetic susceptibility and specific heat data with multi-exchange Heisenberg models, using high temperature series expansions (HTSE). The 10th-order cubic $J_1 - J_2 - J_3$ HTSE (first, second, third nearest-neighbors) failed to reproduce the data. A good agreement is achieved by including couplings up to the second nearest-neighbors and a tetragonal distortion along the c axis, namely

$$\hat{\mathcal{H}} = J_1 \sum_{\langle i, j \rangle} \hat{\mathbf{S}}_i \cdot \hat{\mathbf{S}}_j + J_c \sum_{\langle\langle i, j \rangle\rangle_c} \hat{\mathbf{S}}_i \cdot \hat{\mathbf{S}}_j + J_{ab} \sum_{\langle\langle i, j \rangle\rangle_{a,b}} \hat{\mathbf{S}}_i \cdot \hat{\mathbf{S}}_j. \tag{3}$$

In Eq. 3, $\langle i, j \rangle$ denote first nearest-neighbors (1st NN), while $\langle\langle i, j \rangle\rangle_{a,b,c}$ corresponds to second nearest-neighbor (2nd NN) along the a , b or c axis. The data were reproduced down to $T = 10$ K using pade approximant of the 12th-order HTSE for the susceptibility and 13th-order HTSE for the specific heat (Fig. 4a). See Methods details on the procedure. Based on our best fit, the exchange parameters are $J_1 = 4.75$ K, $J_{ab} = 7.25$ K, and $J_c = -23.25$ K. Clearly, the small tetragonal distortion greatly affects the magnetic properties of $\text{NaCa}_2\text{Cu}_2(\text{VO}_4)_3$: the strongly ferromagnetic J_c interaction promotes ferromagnetic spin chains along the c axis, yet frustrated by the competing antiferromagnetic J_1 and J_{ab} couplings.

This result is consistent with our polarized neutron diffraction measurements. Indeed, we found AF correlations for 1st NN and weaker F correlations for 2nd NN, reflecting the partial averaging of strong F exchange along the c axis and weaker AF exchange along the a, b axis.

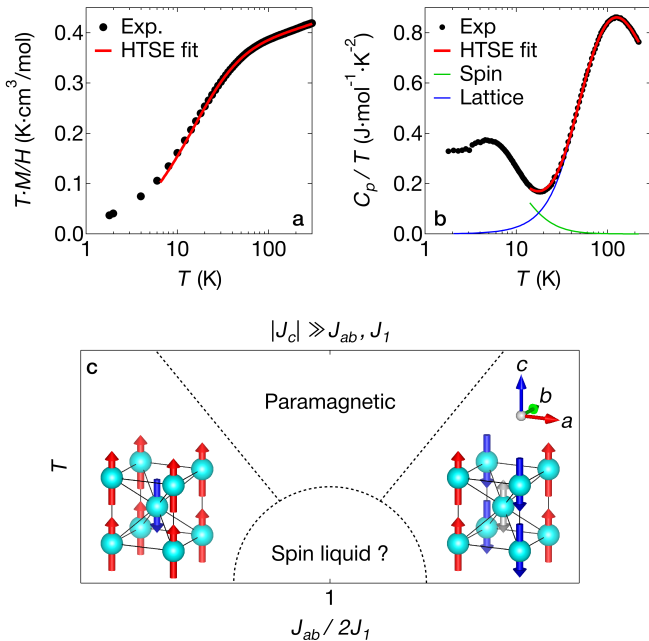


FIG. 4. **Numerical analysis of $\text{NaCa}_2\text{Cu}_2(\text{VO}_4)_3$ magnetic properties from high-temperature series expansion (HTSE).** **a** Comparison of the magnetic susceptibility measured with $\mu_0 H = 5$ T (black dots) and the HTSE fit down to $T = 10$ K (red line). **b** Total specific heat measured in zero-field (black dots), with the model (red line) consisting of a lattice contribution (blue line, see methods) and a spin contribution (green line) fitted from the HTSE down to $T = 10$ K. **c** Schematic phase diagram of the spin model of Eq. 3 for a dominant ferromagnetic J_c . The exchange parameters of $\text{NaCa}_2\text{Cu}_2(\text{VO}_4)_3$ extracted from the HTSE place it near $J_{ab}/2J_1 \sim 1$.

DISCUSSION

Our exchange values suggest significant magnetic frustration between J_1 and J_{ab} . Indeed, assuming ferromagnetic chains along the c axis, two magnetic orders (illustrated in Fig. 4b) compete. If the coupling J_1 between the two sublattices dominates, both cubic sublattices order ferromagnetically while the order between them is antiferromagnetic. Conversely, if the interchain coupling J_{ab} is stronger, neighboring chains within each sublattice order antiferromagnetically while the mean field of one sublattice on the other one cancels out. Crucially, because each spin is surrounded by 8 others coupled with J_1 and 4 others coupled with J_{ab} , the ratio $J_{ab}/2J_1$ determines the balance of the two interactions. In our case, this value is rather close to unity ($J_{ab}/2J_1 \simeq 0.76$), highlighting the strong frustration among these competing exchange paths. Although a direct comparison with the bcc calculations of Refs. [43, 44] is difficult due to the small tetragonal distortion present in $\text{NaCa}_2\text{Cu}_2(\text{VO}_4)_3$, we note that the quantum paramagnetic region of their phase diagram lies between the two magnetic orders

described above (corresponding to those identified as $(2\pi, 0, 0)$ and $(\pi, \pi, 0)$). Thus, the frustration induced spin liquid state of $\text{NaCa}_2\text{Cu}_2(\text{VO}_4)_3$ suggested in the schematic phase diagram in Fig. 4b is certainly related to their quantum disordered state.

The presence of strong 1D correlations in $\text{NaCa}_2\text{Cu}_2(\text{VO}_4)_3$ was already pointed out in early studies [42] based on the analysis of bulk macroscopic measurements. However, these correlations were believed to be antiferromagnetic in nature. This interpretation was difficult to reconcile with simple theoretical models, and the qualitative disagreement between the data and the models was attributed to correlated chains of variable lengths due to complex Jahn-Teller effects. Our analysis provides new insight into this issue, offering compelling evidence for ferromagnetically correlated chains along the c axis, which are coupled antiferromagnetically to the neighboring chains of both the sublattices. However, as demonstrated by our μSR measurements, spin-lattice effects are at play down to the lowest measured temperature of $T = 50$ mK. The orbital overlap - and hence the exchange coupling - could still vary well below $T = 10$ K, highlighting the need for comprehensive studies of the strongly magnetically correlated state of $\text{NaCa}_2\text{Cu}_2(\text{VO}_4)_3$ at dilution temperatures.

In summary, we demonstrated using a combination of macroscopic measurements, neutron scattering and muon spin relaxation techniques, that the nearly cubic, magnetically correlated, $S = 1/2$ system $\text{NaCa}_2\text{Cu}_2(\text{VO}_4)_3$ remains dynamic down to at least $T = 50$ mK while it becomes correlated in a temperature range two orders of magnitude higher. We were able to account for this behavior through numerical simulations including the Jahn-Teller driven structural distortion. This yielded three relevant exchange interactions responsible for correlated ferromagnetic chains as well as strong frustration between them. This scenario of a spin-lattice coupling induced frustration provides a first but compelling explanation for the absence of magnetic order down to 50 mK and the stabilization of the intriguing three-dimensional spin liquid state of $\text{NaCa}_2\text{Cu}_2(\text{VO}_4)_3$.

METHODS

Sample synthesis

In order to prepare the polycrystalline samples of $\text{NaCa}_2\text{Cu}_2(\text{VO}_4)_3$, high purity oxide materials of Na_2CO_3 , CaCO_3 , CuO , and V_2O_5 were mixed in stoichiometry and the mixture was pelletized and heat treated in the temperature range 500°C to 720°C for twelve hours at each temperature with several intermittent grindings. The estimated lattice parameters from the Rietveld refined data are in excellent agreement with the literature reported values [35].

Details on the data analysis

The bcc lattice contribution to the specific heat (Fig. 1f) was extracted from measurements of the non-magnetic system $\text{NaCa}_2\text{Mg}_2(\text{VO}_4)_3$. The method described in Ref. [51] was used to account for the difference in molar mass between Cu and Mg.

We fitted the temperature dependence of the specific heat subtracted from the bcc lattice contributions and divided by the temperature by two phenomenological log-normal distributions. They represent the magnetic and Jahn-Teller parts of the specific heat, and are defined as

$$f(T) = \frac{A}{T\sigma\sqrt{2\pi}} \exp\left(\frac{-(\ln(T) - \mu)^2}{2\sigma^2}\right) \quad (4)$$

with A their area and σ, μ two parameters. These distributions were chosen for their asymmetry and null limits in both low and high temperatures. For the magnetic part, our fits give $A_{\text{Mag}} = 5.50$, $\sigma_{\text{Mag}} = 0.92$ and $\mu_{\text{Mag}} = 2.25$. For the Jahn-Teller part, we obtained $A_{\text{JT}} = 3.05$, $\sigma_{\text{JT}} = 0.47$ and $\mu_{\text{JT}} = 4.26$.

The constant momentum cuts (shown in Figs. 3c,f and Supplementary Information C) were obtained by combining the data measured with $E_i = 3.7$ meV and $E_i = 12.12$ meV. We first integrated the measured intensity for both incident energies in successive windows defined by $Q \pm 0.05 \text{ \AA}^{-1}$, with Q ranging from $Q = 0.55 \text{ \AA}^{-1}$ to $Q = 2.15 \text{ \AA}^{-1}$. The intensity of the cuts obtained with $E_i = 3.7$ meV multiplied by a factor 1.8 overlap the intensity of the cuts obtained with $E_i = 12.12$ meV. Thus, we merged the two sets of data: the resulting by combining the data from $E_i = 3.7$ meV (multiplied by 1.8) between -1.6 meV and 1.8 meV, and the data from $E_i = 12.12$ meV elsewhere. Only the positive part of the merged cuts were fitted, excluding the region $0 \leq E \leq 0.25$ meV dominated by the elastic peak.

The inelastic and quasi-elastic energy integrated intensity, depicted in Figs. 3h,i, were calculated by integrating the fitted quasi-elastic and inelastic contributions of the scattering function $S(E, T)$ between 0 \AA^{-1} and 9 \AA^{-1} . Formally, for each Q corresponding to a constant momentum cut, the inelastic energy integrated intensity A_{Inel} and the quasi-elastic energy integrated intensity A_{Qel} were defined as

$$\begin{aligned} A_{\text{Qel}} &= \int_0^9 \frac{1}{1 - \exp(-E/k_{\text{B}}T)} \chi''_{\text{Qel}}(E) dE; \\ A_{\text{Inel}} &= \int_0^9 \frac{1}{1 - \exp(-E/k_{\text{B}}T)} \chi''_{\text{Inel}}(E) dE; \end{aligned} \quad (5)$$

where $\chi''_{\text{Qel}}(E)$ (resp. $\chi''_{\text{Inel}}(E)$) depends on the parameters z and γ_Q (resp. Z, E_c and Γ) obtained from the fits of the constant momentum scans.

High temperature series expansion

The measured linear susceptibility is defined as $\chi_l^{\text{expe}} = M/\mu_0 H$. For each set of exchange energy $\{J_\alpha\}$, the HTSE of $T\chi_l^{\text{theo}}$ is evaluated and the linear parameters A_χ and B_χ are calculated by minimizing the error E_χ :

$$E_\chi = \sum_{T_i > T_{\text{min}}} (T_i \chi_l^{\text{expe}}(T_i) - A_\chi T_i \chi_l^{\text{theo}}(T_i) - B_\chi T_i)^2, \quad (6)$$

where T_{min} is the lowest temperature where at least 6 pade approximants of the HTSE of $T\chi_l^{\text{theo}}$ differ by less than 0.001 (T_{min} is evaluated for each set $\{J_\alpha\}$). B_χ is essential to account for some residual constant contribution and a small value less than 10^{-4} is expected.

The specific heat has a spin contribution and a phonon or lattice contribution. The phonon contribution is represented here by 3 modes (more do not help):

$$C_p^{\text{phonon}}(T) = \sum_{k=1}^3 W_k P\left(\frac{T_{D,k}}{T}\right), \quad (7)$$

$$P(x) = 9 \left(\frac{4}{3} D_3(x) - \frac{x}{\exp(x) - 1} \right), \quad (8)$$

$$D_3(x) = \frac{3}{x^3} \int_0^x dt \frac{t^3}{e^t - 1}. \quad (9)$$

The error on C_p of the model is measured by E_C :

$$E_C = \sum_{T_i > T_{\text{min}}} (C_p^{\text{expe}} - A_C C_p^{\text{spin}} - C_p^{\text{phonon}}(T))^2, \quad (10)$$

where T_{min} is the the lowest temperature where at least 6 pade approximants of the HTSE of C_p^{spin} differ by less than 0.001. A_C and W_k are linear parameters, and $T_{D,k}$ non linear ones.

The set $\{J_\alpha\}$ of exchange energies varies on a grid of step $0.25 K$, running from $-50 K$ to $50 K$. For each $\{J_\alpha\}$, χ_l^{theo} and C_p^{spin} are evaluated at the temperature of experiments. Then A_χ, B_χ, A_C, W_k , and $T_{D,k}$ are calculated by minimizing E_χ and E_C . The total error of such fit is $E_\chi + E_C$. The best fit minimizes this total error. We found that the phonon Debye temperatures stay close to 300 K and 600 K for the two lowest temperatures whereas the last temperature is much higher around 3000 K. The respective weights W_k are close to 28, 38 and 120.

ACKNOWLEDGMENTS

Y. A. thank V. Simonet and E. Lhotel for fruitful discussions. E. K. acknowledges very useful discussions with H. O. Jeschke and Y. Iqbal. Experiments at the ISIS Neutron and Muon Source were supported by a beamtime allocation RB2410480 from the Science and Technology Facilities Council. Data is available here: <https://doi.org/10.5286/ISIS.E.RB2410480>. This work was supported by the French Agence Nationale

de la Recherche, under Grant No. ANR- 18-CE30-0022 “LINK”. E. K. and R. S. acknowledge financial support from the labex PALM for the QuantumPyroMan project (ANR-10-LABX-0039-PALM).

* yann.alexanian@unige.ch; current address: Department of Quantum Matter Physics, University of Geneva, CH-1211 Geneva, Switzerland

- [1] C. Lacroix, P. Mendels, and F. Mila, eds., *Introduction to Frustrated Magnetism: Materials, Experiments, Theory* (Springer, Berlin London, 2011).
- [2] L. Balents, Spin liquids in frustrated magnets, *Nature* **464**, 199 (2010).
- [3] C. Broholm, R. J. Cava, S. A. Kivelson, D. G. Nocera, M. R. Norman, and T. Senthil, Quantum spin liquids, *Science* **367**, 6475 (2020).
- [4] F. Haldane, Continuum dynamics of the 1-D heisenberg antiferromagnet: Identification with the O(3) nonlinear sigma model, *Physics Letters A* **93**, 464 (1983).
- [5] F. D. M. Haldane, Nonlinear field theory of large-spin heisenberg antiferromagnets: Semiclassically quantized solitons of the one-dimensional easy-axis néel state, *Physical Review Letters* **50**, 1153 (1983).
- [6] U. Schollwöck, J. Richter, D. J. J. Farnell, and R. F. Bishop, eds., *Quantum Magnetism* (Springer Berlin Heidelberg, 2004).
- [7] T. Giamarchi, *Quantum Physics in One Dimension* (Clarendon Press, 2004).
- [8] P. Mendels and F. Bert, Quantum kagome frustrated antiferromagnets: One route to quantum spin liquids, *Comptes Rendus. Physique* **17**, 455 (2015).
- [9] Y. Li, P. Gegenwart, and A. A. Tsirlin, Spin liquids in geometrically perfect triangular antiferromagnets, *Journal of Physics: Condensed Matter* **32**, 224004 (2020).
- [10] P. Khuntia, M. Velazquez, Q. Barthélemy, F. Bert, E. Kermarrec, A. Legros, B. Bernu, L. Messio, A. Zorko, and P. Mendels, Gapless ground state in the archetypal quantum kagome antiferromagnet $\text{ZnCu}_3(\text{OH})_6\text{Cl}_2$, *Nature Physics* **16**, 469 (2020).
- [11] P. Mendels, F. Bert, M. A. de Vries, A. Olariu, A. Harrison, F. Duc, J. C. Trombe, J. S. Lord, A. Amato, and C. Baines, Quantum magnetism in the paratacamite family: Towards an ideal kagomé lattice, *Physical Review Letters* **98**, 077204 (2007).
- [12] T.-H. Han, J. S. Helton, S. Chu, D. G. Nocera, J. A. Rodriguez-Rivera, C. Broholm, and Y. S. Lee, Fractionalized excitations in the spin-liquid state of a kagome-lattice antiferromagnet, *Nature* **492**, 406 (2012).
- [13] Y. Okamoto, M. Nohara, H. Aruga-Katori, and H. Takagi, Spin-liquid state in the $S = 1/2$ hyperkagome antiferromagnet $\text{Na}_4\text{Ir}_3\text{O}_8$, *Physical Review Letters* **99**, 137207 (2007).
- [14] J. Khatua, S. Bhattacharya, Q. P. Ding, S. Vrtnik, A. M. Strydom, N. P. Butch, H. Luetkens, E. Kermarrec, M. S. R. Rao, A. Zorko, Y. Furukawa, and P. Khuntia, Spin liquid state in a rare-earth hyperkagome lattice, *Physical Review B* **106**, 104404 (2022).
- [15] M. Subramanian, G. Aravamudan, and G. Subba Rao, Oxide pyrochlores — a review, *Progress in Solid State Chemistry* **15**, 55 (1983).
- [16] J. S. Gardner, M. J. P. Gingras, and J. E. Greedan, Magnetic pyrochlore oxides, *Reviews of Modern Physics* **82**, 53 (2010).
- [17] I. Živković, V. Favre, C. Salazar Mejia, H. O. Jeschke, A. Magrez, B. Dabholkar, V. Nocolak, R. S. Freitas, M. Jeong, N. G. Hegde, L. Testa, P. Babkevich, Y. Su, P. Manuel, H. Luetkens, C. Baines, P. J. Baker, J. Wosnitzer, O. Zaharko, Y. Iqbal, J. Reuther, and H. M. Rønnow, Magnetic field induced quantum spin liquid in the two coupled trillium lattices of $\text{K}_2\text{Ni}_2(\text{SO}_4)_3$, *Physical Review Letters* **127**, 157204 (2021).
- [18] J. M. Bulled, J. A. Paddison, A. Wildes, E. Lhotel, S. J. Cassidy, B. Pato-Doldán, L. C. Gómez-Aguirre, P. J. Saines, and A. L. Goodwin, Geometric frustration on the trillium lattice in a magnetic metal-organic framework, *Physical Review Letters* **128**, 177201 (2022).
- [19] K. Boya, K. Nam, K. Kargeti, A. Jain, R. Kumar, S. K. Panda, S. M. Yusuf, P. L. Paulose, U. K. Voma, E. Kermarrec, K. H. Kim, and B. Koteswararao, Signatures of spin-liquid state in a 3D frustrated lattice compound $\text{KSrFe}_2(\text{PO}_4)_3$ with $S = 5/2$, *APL Materials* **10**, 101103 (2022).
- [20] R. Moessner and J. T. Chalker, Properties of a classical spin liquid: The heisenberg pyrochlore antiferromagnet, *Physical Review Letters* **80**, 2929 (1998).
- [21] B. Canals and C. Lacroix, Pyrochlore antiferromagnet: A three-dimensional quantum spin liquid, *Physical Review Letters* **80**, 2933–2936 (1998).
- [22] J. M. Hopkinson and H.-Y. Kee, Geometric frustration inherent to the trillium lattice, a sublattice of the B20 structure, *Physical Review B* **74**, 224441 (2006).
- [23] J. M. Hopkinson, S. V. Isakov, H.-Y. Kee, and Y. B. Kim, Classical antiferromagnet on a hyperkagome lattice, *Physical Review Letters* **99**, 037201 (2007).
- [24] L. Savary and L. Balents, Disorder-induced quantum spin liquid in spin ice pyrochlores, *Physical Review Letters* **118**, 087203 (2017).
- [25] M.-H. Li, S. Biswas, and S. Parameswaran, Classification of spin-1/2 fermionic quantum spin liquids on the trillium lattice, [arXiv:2409.02898](https://arxiv.org/abs/2409.02898).
- [26] J. G. Rau and M. J. Gingras, Frustrated quantum rare-earth pyrochlores, *Annual Review of Condensed Matter Physics* **10**, 357 (2019).
- [27] E. Smith, O. Benton, D. Yahne, B. Placke, R. Schäfer, J. Gaudet, J. Dudemaine, A. Fitterman, J. Beare, A. Wildes, S. Bhattacharya, T. DeLazzer, C. Buhariwalla, N. Butch, R. Movshovich, J. Garrett, C. Marjerrison, J. Clancy, E. Kermarrec, G. Luke, A. Bianchi, K. Ross, and B. Gaulin, Case for a $U(1)_\pi$ quantum spin liquid ground state in the dipole-octupole pyrochlore $\text{Ce}_2\text{Zr}_2\text{O}_7$, *Physical Review X* **12**, 021015 (2022).
- [28] V. Porée, H. Yan, F. Desrochers, S. Petit, E. Lhotel, M. Appel, J. Ollivier, Y. B. Kim, A. H. Nevidomskyy, and R. Sibille, Evidence for fractional matter coupled to an emergent gauge field in a quantum spin ice, *Nature Physics* [10.1038/s41567-024-02711-w](https://doi.org/10.1038/s41567-024-02711-w) (2024).
- [29] R. Sibille, E. Lhotel, M. Ciomaga Hatnean, G. J. Nilssen, G. Ehlers, A. Cervellino, E. Ressouche, M. Frontzek, O. Zaharko, V. Pomjakushin, U. Stuhr, H. C. Walker, D. T. Adroja, H. Luetkens, C. Baines, A. Amato, G. Balakrishnan, T. Fennell, and M. Kenzelmann, Coulomb spin liquid in anion-disordered pyrochlore $\text{Tb}_2\text{Hf}_2\text{O}_7$, *Nature Communications* **8**, 892 (2017).

- [30] Y. Alexanian, E. Lhotel, R. Ballou, C. V. Colin, H. Klein, A. Le Priol, F. Museur, J. Robert, E. Pachoud, P. Lejay, A. Hadj-Azzem, B. Fåk, Q. Berrod, J.-M. Zanotti, E. Suard, C. Dejoie, S. de Brion, and V. Simonet, Collective magnetic state induced by charge disorder in the non-kramers rare-earth pyrochlore Tb_2ScNbO_7 , *Physical Review Materials* **7**, 094403 (2023).
- [31] C. Balz, B. Lake, J. Reuther, H. Luetkens, R. Schönemann, T. Herrmannsdörfer, Y. Singh, A. T. M. Nazmul Islam, E. M. Wheeler, J. A. Rodriguez-Rivera, T. Guidi, G. G. Simeoni, C. Baines, and H. Ryll, Physical realization of a quantum spin liquid based on a complex frustration mechanism, *Nature Physics* **12**, 942 (2016).
- [32] C. Balz, B. Lake, A. T. M. Nazmul Islam, Y. Singh, J. A. Rodriguez-Rivera, T. Guidi, E. M. Wheeler, G. G. Simeoni, and H. Ryll, Magnetic hamiltonian and phase diagram of the quantum spin liquid $Ca_{10}Cr_7O_{28}$, *Physical Review B* **95**, 174414 (2017).
- [33] B. Koteswararao, R. Kumar, P. Khuntia, S. Bhowal, S. K. Panda, M. R. Rahman, A. V. Mahajan, I. Dasgupta, M. Baenitz, K. H. Kim, and F. C. Chou, Magnetic properties and heat capacity of the three-dimensional frustrated antiferromagnet, *Physical Review B* **90**, 035141 (2014).
- [34] P. Khuntia, F. Bert, P. Mendels, B. Koteswararao, A. Mahajan, M. Baenitz, F. Chou, C. Baines, A. Amato, and Y. Furukawa, Spin liquid state in the 3d frustrated antiferromagnet $PbCuTeO_6$: NMR and Muon Spin Relaxation studies, *Physical Review Letters* **116**, 107203 (2016).
- [35] G. Bayer, Vanadates $A_3B_2V_3O_{12}$ with garnet structure, *Journal of the American Ceramic Society* **48**, 600 (1965).
- [36] S. Geller, Crystal chemistry of the garnets, *Zeitschrift für Kristallographie - Crystalline Materials* **125**, 1 (1967).
- [37] J. A. Lussier, B. N. Richtig, C. Mauws, J. W. Lynn, and C. R. Wiebe, Absence of magnetic ordering in the spin liquid candidate $Ca_3Cu_2GeV_2O_{12}$, *Journal of Physics: Condensed Matter* **32**, 134001 (2019).
- [38] Z. A. Kazei, B. V. Mill', and V. I. Sokolov, Cooperative jahn-teller effect in the garnet $Ca_3Mn_2Ge_3O_{12}$, *Pis'ma Zh. Eksp. Teor. Fiz.* **24**, 229 (1976).
- [39] Z. A. Kazei, P. Novak, and V. I. Sokolov, Peculiarities of the metamagnetic transition of a garnet single crystal $Ca_3Mn_2Ge_3O_{12}$, *Pis'ma Zh. Eksp. Teor. Fiz.* **31**, 338 (1980).
- [40] Z. A. Kazei, P. Novak, and V. I. Sokolov, Cooperative jahn-teller effect in the garnets, *Zh. Eksp. Teor. Fiz.* **83**, 1483 (1982).
- [41] E. F. Shender, Antiferromagnetic garnets with fluctuationally interacting sublattices, *Zh. Eksp. Teor. Fiz.* **83**, 326 (1982).
- [42] Z. A. Kazei, P. Novak, and V. I. Sokolov, Quasi-one-dimensional nature of magnetic ordering due to the cooperative jahn-teller effect in the garnet $NaCa_2Cu_2V_3O_{12}$ (CuVG), *Pis'ma Zh. Eksp. Teor. Fiz.* **38**, 281 (1983).
- [43] P. Ghosh, T. Müller, F. P. Toldin, J. Richter, R. Narayanan, R. Thomale, J. Reuther, and Y. Iqbal, Quantum paramagnetism and helimagnetic orders in the heisenberg model on the body centered cubic lattice, *Physical Review B* **100**, 014420 (2019).
- [44] J. Sonnenschein, A. Chauhan, Y. Iqbal, and J. Reuther, Projective symmetry group classifications of quantum spin liquids on the simple cubic, body centered cubic, and face centered cubic lattices, *Physical Review B* **102**, 125140 (2020).
- [45] J. A. M. Paddison, J. Ross Stewart, and A. L. Goodwin, spinvert: a program for refinement of paramagnetic diffuse scattering data, *Journal of Physics: Condensed Matter* **25**, 454220 (2013).
- [46] J. A. M. Paddison, Ultrafast calculation of diffuse scattering from atomistic models, *Acta Crystallographica Section A Foundations and Advances* **75**, 14 (2019).
- [47] A. Yaouanc and P. D. de Réotier, eds., *Muon Spin Rotation, Relaxation and Resonance: Applications to Condensed Matter* (Oxford University Press, Oxford, 2011).
- [48] D. R. Noakes and G. M. Kalvius, Anomalous zero-field muon spin relaxation in highly disordered magnets, *Phys. Rev. B* **56**, 2352 (1997).
- [49] B. Fåk, E. Kermarrec, L. Messio, B. Bernu, C. Lhuillier, F. Bert, P. Mendels, B. Koteswararao, F. Bouquet, J. Ollivier, A. D. Hillier, A. Amato, R. H. Colman, and A. S. Wills, Kapellasite: A kagome quantum spin liquid with competing interactions, *Physical Review Letters* **109**, 037208 (2012).
- [50] S. Chillal, Y. Iqbal, H. O. Jeschke, J. A. Rodriguez-Rivera, R. Bewley, P. Manuel, D. Khalyavin, P. Steffens, R. Thomale, A. T. M. N. Islam, J. Reuther, and B. Lake, Evidence for a three-dimensional quantum spin liquid in $PbCuTe_2O_6$, *Nature Communications* **11**, 2348 (2020).
- [51] V. Hardy, S. Lambert, M. R. Lees, and D. McK. Paul, Specific heat and magnetization study on single crystals of the frustrated quasi-one-dimensional oxide $Ca_3Co_2O_6$, *Physical Review B* **68**, 014424 (2003).

Supplementary Information for "Three-dimensional spin liquid state in the frustrated $S = 1/2$ Heisenberg garnet $\text{NaCa}_2\text{Cu}_2(\text{VO}_4)_3$ "

Y. Alexanian,^{1,*} R. Kumar,² H. Zeroual,² B. Bernu,³ L. Mangin-Thro,¹ R. S. Stewart,⁴
J. M. Wilkinson,⁴ P. L. Paulose,⁵ F. Bert,² P. Mendels,² B. Fåk,¹ and E. Kermarrec²

¹*Institut Laue Langevin, 38042 Grenoble, France*

²*Université Paris-Saclay, CNRS, Laboratoire de Physique des Solides, 91405, Orsay, France*

³*Sorbonne Université, CNRS, Laboratoire de Physique Théorique de la Matière Condensée, 75252 Paris Cedex 05, France*

⁴*ISIS Neutron and Muon Source, Rutherford Appleton Laboratory, Didcot OX11 0QX, United Kingdom*

⁵*Department of Condensed Matter Physics and Materials Science, TIFR, Mumbai 400 005, India*

(Dated: January 9, 2025)

A. CRISTALLOGRAPHIC STRUCTURE

X-ray diffractograms of our $\text{NaCa}_2\text{Cu}_2(\text{VO}_4)_3$ polycrystalline samples measured at $T = 298$ K are shown in Fig. S1a. The refinement of the diffractogram confirm a cubic garnet structure shown in Fig. S1b (space group $n^\circ 230$ $\text{Ia}\bar{3}\text{d}$, 8 formula per unit cell). We found a unit cell parameter $a = b = c = 12.425$ Å, in very good agreement with previous studies [40, 42]. Other refined free parameters and description of the structure is given in Table S1. In particular, we confirm that the magnetic Cu atoms sits in a body centered cubic (bcc) lattice.

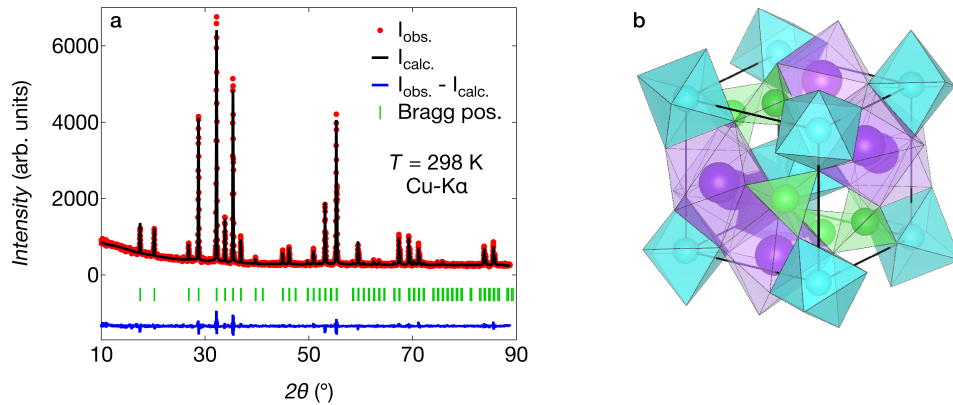


FIG. S1. **Structural characterizations of $\text{NaCa}_2\text{Cu}_2(\text{VO}_4)_3$.** **a** X-ray diffractograms of polycrystalline $\text{NaCa}_2\text{Cu}_2(\text{VO}_4)_3$ at room temperature (red dots). Rietveld refinement of the data in the space group $n^\circ 230$ $\text{Ia}\bar{3}\text{d}$ is shown in black and the difference between refinement and data in yellow. The Bragg peak positions are indicated by blue ticks. **b** 1/8 of the cubic unit cell of $\text{NaCa}_2\text{Cu}_2(\text{VO}_4)_3$. $\text{Na}^+/\text{Ca}^{2+}$ (24c), Cu^{2+} (16a) and V^{5+} (24d) ions are purple, blue, and green respectively. Oxygens O^{2-} (96h) landing at the vertices of the different polyhedra are not shown explicitly.

Atom	Na / Ca	Cu	V	O
Wyckoff	24c	16a	24d	96h
Symm.	222	$\bar{3}$	$\bar{4}$	1
x	0	0	0	-0.0394
y	1/4	0	1/4	0.0541
z	1/8	0	3/8	0.1563
Occ.	0.333 / 0.667	1	1	1
Poly.	Dodecahedron	Octahedron	Tetrahedron	n.a.

TABLE S1. Results of the Rietvelt refinement of $\text{NaCa}_2\text{Cu}_2(\text{VO}_4)_3$ from X-ray diffraction data in the $\text{Ia}\bar{3}\text{d}$ ($n^\circ 230$) space group at $T = 298$ K. The refined unit cell parameter is 12.425 Å.

B. COMPLEMENT ON THE ANALYSIS OF POLARIZED NEUTRON DIFFRACTION

In Fig. S2, we present a comparison of the polarized neutron diffraction results at $T = 1.5$ K and $T = 300$ K. Oscillations in the intensity are clearly visible at low temperatures, but are no longer present at room temperature. This indicates that the system is uncorrelated (paramagnetic) at $T = 300$ K.

The expected magnetic diffuse scattering of $\text{NaCa}_2\text{Cu}_2(\text{VO}_4)_3$ is shown in Fig. S3a,b in the $(hk0)$ and (hhl) scattering planes, respectively. These patterns were calculated using the software SCATTY, which reconstructs the single crystal magnetic diffuse scattering from the Monte-Carlo simulations of the powder data obtained with SPINVERT.

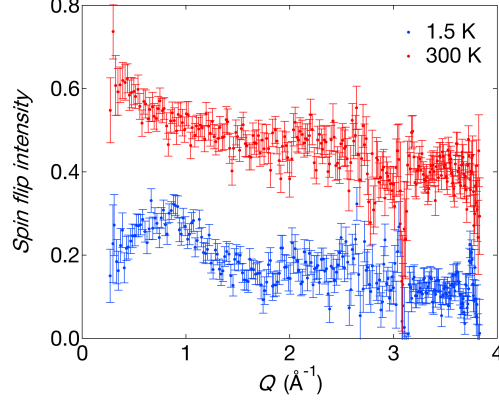


FIG. S2. **Polarized neutron diffraction results.** Data at $T = 1.5$ K are shown in blue, while data at $T = 300$ K are shown in red.

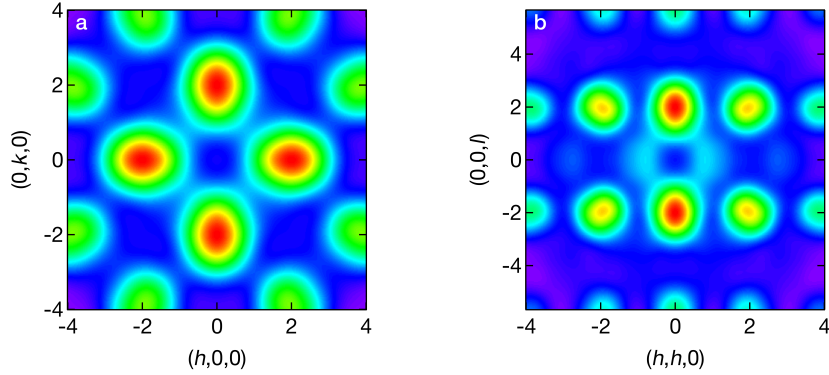


FIG. S3. **Magnetic diffuse scattering calculated with SCATTY.** **a** In the $(hk0)$ plane. **b** In the (hhl) plane.

C. FITS OF THE CONSTANT MOMENTUM CUTS FROM INELASTIC NEUTRON SCATTERING

Constant momentum cuts for different Q values (each integrated over a range $Q \pm 0.05 \text{ \AA}^{-1}$) and their corresponding fits are shown in Fig. S4a for $T = 1.5$ K and Fig. S4b for $T = 20$ K. As described in main text, the data were fitted using the scattering function

$$S(E, T) = \frac{1}{1 - \exp(-E/k_B T)} \left[\frac{z\gamma_Q E}{E^2 + \gamma^2} + \left(\frac{Z\Gamma}{(E - E_c)^2 + \Gamma^2} - \frac{Z\Gamma}{(E + E_c)^2 + \Gamma^2} \right) \right] \quad (\text{S1})$$

which represents the sum of a quasi-elastic and an inelastic contributions. The fits show excellent agreement with the data at both temperatures and for all momentum values Q ranging from $Q = 0.55 \text{ \AA}^{-1}$ to $Q = 2.15 \text{ \AA}^{-1}$. The parameters E_c , Γ and γ are displayed in Fig. S4c.

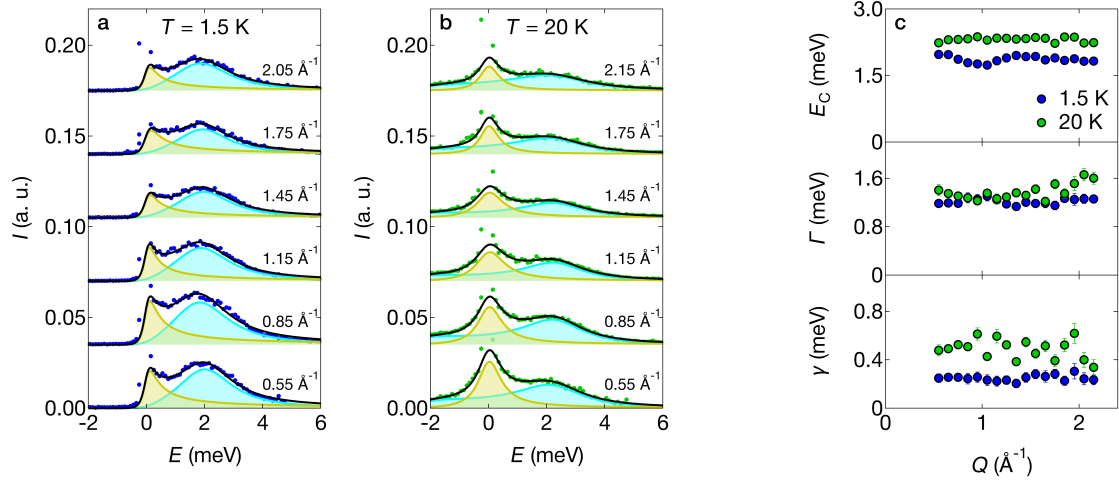


FIG. S4. **Fits of the constant momentum cuts.** **a,b** Constant momentum cuts (dots) with corresponding fits (black line), consisting of a quasi-elastic contribution (yellow area) and an inelastic contribution (blue area) at (a) $T = 1.5$ K and (b) $T = 20$ K. **c** Fit parameters: characteristic energy of the inelastic contribution (top), half width at half maximum of the inelastic contribution (middle) and half width at half maximum of the quasi-elastic contribution (bottom).